

Prussian Blue Nanoplates for Potassium Ion Battery Cathode with High Capacity and High Energy Density

SungHoon Jung,^[a] Pham Thi Huong,^[a] Mitesh Mapari,^[a] Tran Thanh Tung,^{*[b]} and TaeYoung Kim^{*[a]}

Prussian blue analogues (PBAs) represent as a class of materials with an open framework structure and have been intensively explored as the potential active materials for alkaline-ion batteries. Here, we present the synthesis of Prussian blue nanoplates designed for use as high performance cathode materials in potassium-ion batteries. Prussian blue nanoplates were synthesized through a facile solution precipitation route using a highly concentrated potassium citrate solution. The potassium-rich environment during the synthesis facilitated horizontal growth of the crystals, yielding potassium-rich Prussian blue nanoplates. The resultant Prussian blue nanoplates exhibited a significantly larger particle size of 600 nm and a reduced specific surface area of $6.8 \text{ m}^2 \text{ g}^{-1}$, compared to conventionally synthesized Prussian blue hexahedrons. Half-cell

tests demonstrated that the Prussian blue nanoplates exhibited a high gravimetric capacity of 152.5 mAh g^{-1} with a nominal voltage 3.952 V at a C-rate of 0.1 C, yielding an energy density of 602.7 Wh kg^{-1} . Cycling tests demonstrated high cycling stability of the material, maintaining a capacity of 122.7 mAh g^{-1} and a nominal voltage of 3.923 V after 200 cycles at 0.2 C. In a full-cell configuration with graphite anodes, a gravimetric capacity changed from 134.1 mAh g^{-1} to 108.9 mAh g^{-1} after 100 cycles at 0.2 C, demonstrating a good cycling stability. This work provides a new insight into the electrochemical properties of Prussian blue nanoplates and highlights their potential as high-performance cathode materials for potassium-ion batteries.

Introduction

Potassium-ion batteries (PIBs) or K-ion batteries (KIBs) emerge as a promising next-generation green energy storage technology, driven by their advantageous properties. These include cost-effectiveness derived from the abundance of potassium in the Earth's crust, the potential for achieving high energy density owing to a low standard redox potential of potassium (-2.94 V vs standard hydrogen electrode, SHE), a reduced Stokes radius in organic solvent resulting from weaker Lewis acidity of potassium ion (K^+) and low de-solvation energy, and the practical advantage of utilizing Al foil as current collector that is lighter and less costly than Cu.^[1] As efforts to develop potassium-ion battery progressed, extensive researches focused on the negative electrode materials, revealing that typical graphite material and hard carbons widely utilized in Li-ion batteries (LIBs) can be used to insert and extract potassium ions reversibly.^[1a,2] Layered oxides such as K_xMO_2 ($M=3\text{d}$ transition metals) compounds have been extensively studied as positive electrode materials for aprotic K-ion batteries. Although K_xMO_2 compounds with high capacity have been developed, they

have shown limited performance for KIBs, exhibiting low operating potential ($<3 \text{ V}$ vs K^+/K).^[3] Furthermore, K_xMO_2 compounds have the two-dimensional (2D) diffusion path of alkali metal ions, while open three-dimensional (3D) framework structure of the host material is desirable to accommodate large alkali metals such as K^+ ions.^[3-4] Among the various 3D materials, Prussian blue analogues (PBAs) represented as a $\text{A}_x\text{M1}[\text{M2}(\text{CN})_6]_y\text{nH}_2\text{O}$ (where A is the insertion alkali metal cation, M1 and M2 are transition metals) have 3D open-framework of cyano-perovskite comprised of transition metals bridged by cyanide ligands.^[2a,5] The large interstitial space is derived from an octahedral framework of the M1N_6 and M2C_6 linked via cyano ligand and the framework structure provide an open 3D channel preferable for the diffusion of large K ions to a center of cyano-perovskite crystal with minimal structural change during ion insertion.^[5a] Those cyano-compounds offer advantages such as storing 2 K^+ per formula weight, facile synthetic methods, and easy control over electrochemical properties through substitution of transition metals. Previous studies have demonstrated the use of the iron-coordinated PBAs ($\text{K}_x\text{Fe}[\text{Fe}(\text{CN})_6]_y\text{nH}_2\text{O}$ abbreviated as KFeFe-PBA) as cathode materials in K-ion batteries, exhibiting moderate capacity in the range of $79\text{--}133 \text{ mAh g}^{-1}$.^[1a,2a,5b,c,6] The focus has shifted to manganese-coordinated PBAs ($\text{K}_x\text{Mn}[\text{Fe}(\text{CN})_6]_y\text{nH}_2\text{O}$ abbreviated as KMnFe-PBA) for their relatively higher average potential compared with KFeFe-PBA and higher capacities in the range of $130\text{--}140 \text{ mAh g}^{-1}$, corresponding to $\text{Mn}^{2+/3+}$ redox couple.^[1a,2a,5b]

Although the KMnFe-PBA features high capacity and high average working potential, the reported KMnFe-PBAs often exhibited unsatisfactory long-term cycling performance. KMnFe-

[a] Dr. S. Jung, Dr. P. T. Huong, Mr. M. Mapari, Prof. T. Kim
Department of Material Science Engineering, Gachon University, Seongnam-daero 1342, Seongnam 13120, Republic of Korea
E-mail: taeykim@gachon.ac.kr

[b] Dr. T. Thanh Tung
School of Chemical Engineering, the University of Adelaide, Adelaide, SA 5005, South Australia
E-mail: tran.tung@adelaide.edu.au

 Supporting information for this article is available on the WWW under <https://doi.org/10.1002/batt.202400091>

PBAs are synthesized through a simple coprecipitation method from an aqueous solution of the manganese salts and the hexacyanoferrate precursors, which can result in high vacancy and water content. The empty vacancy can be occupied by water molecules and the high content of interstitial water usually leads to side reactions, shortening the lifetime of KMnFe-PBAs. In this regard, research efforts have been directed towards suppressing vacancies and interstitial water to achieve the high Coulombic efficiency, capacity, nominal voltage, and stable cycling.^[1a,5b] For example, creating potassium-rich environment in the synthesis of PBAs has shown to reduce the percentage of vacancies and residual water within the PBA and minimize the risk from side reactions.^[2a,5a,7] Leigang Xue. *et al.* demonstrated that the synthesis of $K_2Mn[Fe(CN)_6]$ through precipitation of the solution containing K^+ and Na^+ resulted in aggregation of primary particles to large particle with a small specific surface area, which could restrict side reactions.^[5a] Xi Jiang. *et al.* reported a potassium-rich KMnFe-PBAs cathode materials, delivering a capacity of 115 mAh g^{-1} .^[7b] Xiaofei Bie *et al.* reported $K_{1.75}Mn[Fe^{II}(CN)_6]_{0.93} \cdot 0.16H_2O$ prepared by precipitation of precursors in a potassium citrate solution, exhibiting a large specific capacity of 141 mAh g^{-1} and a nominal voltage of 3.8 V .^[8] The K-rich KMnFe-PBAs has demonstrated the gravimetric capacities in the range of $115\text{--}141 \text{ mAh g}^{-1}$ depending on the synthesis conditions, implying a correlation between the content of vacancy and water within the material and the electrochemical performances of the material.

Another critical aspect in achieving superior electrochemical properties of KMnFe-PBA is the control of the morphology and particle size. Due to rapid nucleation, as-precipitated KMnFe-PBA particles often exhibit a fine morphology with a large specific surface area and contain numerous vacancies and defects, which detrimentally affect electrochemical performance by side reactions. Although side reactions from the vacancies and defects could be effectively suppressed through advanced electrolyte modifications such as a molecularly designed phosphate-based electrolyte and ionic liquid-based electrolyte, morphology design is essential for mitigating inherent defects arising from vacancies.^[9] Thus, the morphology design through kinetic control to slow down nucleation and induce near-stoichiometric crystal growth into larger particles may facilitate achieving superior electrochemical performance of KMnFe-PBA and enable high-performance KIBs.

In this study, we present the synthesis of KMnFe-PBA featuring a thin plate-like morphology with a low content of defects and water, which was designed to achieve high capacity, nominal voltage, and good cycling stability. The thin plate-like KMnFe-PBA nanoparticles, referred to as Prussian blue nanoplates (PNP), were synthesized by precipitation of potassium hexacyanoferrate (II) and manganese chloride from highly concentrated potassium citrate solution. The potassium citrate was added to create a K-rich environment for the synthesis and regulate crystal growth rate and direction, resulting in the formation of thin plate-like morphology of KMnFe-PBA. The large particles of the PNPs exhibited a significantly reduced specific surface area, minimizing water-related side effects. In a half-cell configuration, the PNP-based cathodes displayed

exceptional electrochemical performance, with a maximum capacity of 152.5 mAh g^{-1} and a nominal voltage of 3.952 V , leading to a high energy density of 602.7 Wh kg^{-1} . Additionally, the PNP-based cathode demonstrated good cycling stability, maintaining a capacity of 122.7 mAh g^{-1} over 200 cycles. In a full-cell with graphite anodes, the gravimetric capacity changed from 134.1 mAh g^{-1} to 108.9 mAh g^{-1} after 100 cycles, indicating high specific energy and good cycling stability.

Experimental Section

Synthesis of PNPs. Prussian blue nanoplates (PNPs) were synthesized through a precipitation from an aqueous solution of potassium hexacyanoferrate and manganese chloride with potassium citrate solution.^[8] 2 mmol of potassium hexacyanoferrate were dissolved in 100 ml of deionized water under magnetic stirring. 2 mmol of manganese chloride and 4 mmol of potassium citrate were dissolved into 100 ml of deionized water and slowly added dropwise to the potassium hexacyanoferrate solution for 60 min. The resulting mixture exhibited the formation of white suspensions, and the reaction was allowed to continue for 4 h under a nitrogen atmosphere with continuous mixing. After that, the mixed solution was aged for 1 hour at room temperature. The resulting precipitates were collected by centrifugation, washed with deionized water three times, and obtained by vacuum drying at 100°C for 24 h. As comparison, the control KMnFe-PBA sample was synthesized similarly without the addition of potassium citrate, yielding Prussian blue hexadrons (PBHs).

Material Characterization. The morphologies of PNPs were recorded by high-resolution transmission electron microscopy (HR-TEM) on a Tecnai (FEI, USA), and scanning electron microscopy (SEM) on a FEI Quanta 450 FEG. Thermogravimetric analysis (TGA) was conducted using a TA Instrument (SDT Q600, USA) with a heating rate of 4°C min^{-1} to a temperature of 600°C . X-ray diffraction patterns (XRD) were obtained using PANalytical X'pert-pro MPD (Netherlands). The specific surface area (SSA) and pore distribution of the samples were determined through nitrogen (N_2) adsorption and desorption at 77 K , employing a gas adsorption/desorption analyzer (BELSORP-max, Microtrac BEL Corp., Japan). Prior to the N_2 adsorption/desorption measurements, the samples were degassed at 110°C under vacuum for 12 h. The SSA of the samples was calculated using the Brunauer-Emmett-Teller (BET) method, and the pore distribution was analyzed using Barrett-Joyner-Halenda (BJH) method.

Electrochemical Characterization. The electrochemical behavior of the Prussian blue analogues (PBAs) electrodes was evaluated adopting a standard CR2032 coin cell. Electrochemical tests were performed using both half-cell and full-cell configurations. The PBAs were blended into a slurry with carbon black and polyvinylidene fluoride (PVDF) binder in a weight ratio of 7:2:1, respectively. The resulting slurry was coated onto aluminum foil, rolled into a thin sheet, punched into circular disc with a diameter of 14 mm, and dried in a vacuum oven at 100°C for 24 h. The typical electrode density was $\sim 1.0 \text{ mg cm}^{-2}$. The electrodes were paired with K-metal as counter and reference electrode. The electrolyte used for testing was $0.7 \text{ M } KPF_6$ in EC:DEC (1:1, v/v %). For the full-cell, natural graphite (SNO3, SEC carbon, Japan) were used for the anodes. The cathode and anode were prepared in a weight ratio of the 1:0.6, respectively. All cells were assembled in an argon-filled glove box.

Results and Discussion

The Prussian blue nanoplates (PNPs) were synthesized through a direct coprecipitation reaction in an aqueous solution containing potassium hexacyanoferrate, potassium citrate, and manganese chloride, as schematically illustrated in Figure 1. Briefly, solution A was prepared by dissolving 2 mmol of potassium hexacyanoferrate and 4 mmol of potassium citrate in 100 mL of deionized water. Subsequently, a manganese chloride solution prepared by dissolving 2 mmol in 100 mL was added dropwise into solution A under vigorous stirring. The high concentration of potassium citrate in the solution played a crucial role by controlling the nucleation and growth rate of the crystal. In the precipitation reaction, the potassium rich environment also regulates the particle size and morphology, effectively suppressing particle growth in the vertical direction, yielding a potassium manganese hexacyanoferrate (KMnFe-PBA) powders with a thin plate-like morphology

The transmission electron microscopy (TEM) image (Figure 2, a) reveals that thin plate-like KMnFe-PBA nanoparticles (Prussian blue nanoplates, PNP) are predominantly stacked on each other, exhibiting the primary particle size in the range of 400–600 nm. In contrast, the KMnFe-PBA powders precipitated in the solution absent of potassium citrate (Prussian blue hexahedrons, PBH) showed much finer primary particles with a size of 80 nm. (Figure S1, a) This indicates that PNPs precipitated in the highly concentrated potassium citrate solution are at least 3 times larger than PBHs precipitated in the solution without potassium citrate solution (Figure S1, a). TEM image shows that the PNPs are composed of thin layered-octahedral crystals (Figure 2, b), and atomic force microscopy (AFM) images indicates that PNPs are composed of each thin layered-particles with a thickness in the tens of nanometer, in contrast to hexahedron-like nanoparticles characterized by higher height (Figure S1, a, b). A selected area electron diffraction (SAED) pattern showed clear diffraction spots indicative of a homoge-

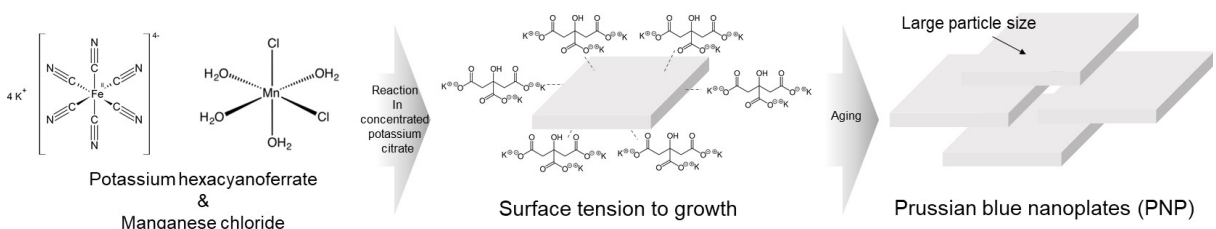


Figure 1. Schematic illustration of Prussian blue nanoplates via precipitation methods.

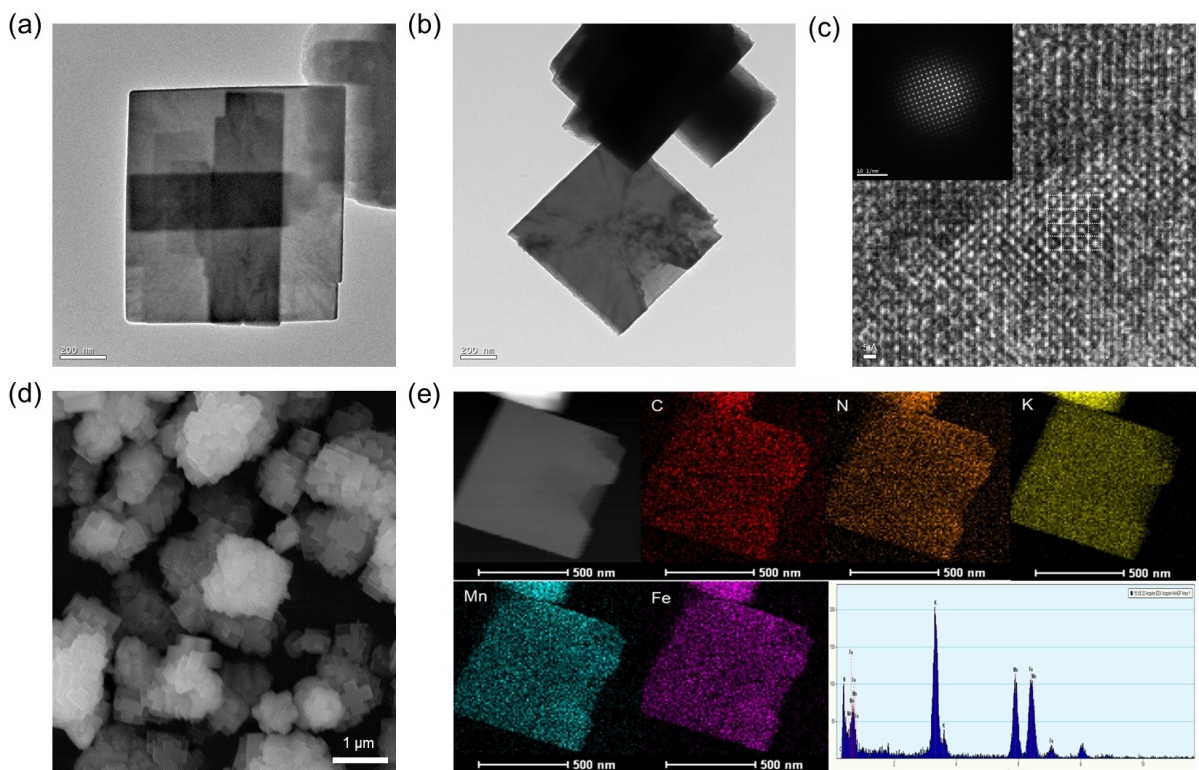


Figure 2. Morphological characterization of PNPs: HR-TEM images (a-c, scale bar: 200, 200, 0.5 nm) in different magnification (inset of c indicates SAED pattern), SEM image (d, scale bar: 1 μ m) and TEM image and the corresponding elemental mapping for C, N, K, Mn, and Fe (e, scale bar: 500 nm).

neous single-crystal structure and high-resolution TEM images also showed potassium ions accommodating in the octahedral frameworks, implying excellent K-ion movement in cathodic reactions (Figure 2, c). Scanning electron microscopy (SEM) image (Figure 2, d) firmly present the large particle size of PNPs, and plate-like nanoparticles implies a smaller specific surface area than that of the hexahedron particles (Figure S3, a-d). Energy dispersive spectroscopy (EDS) spectrum of PNPs was employed to identify the presence and absence of element of PNPs, as presented in Figure 2, e. The elemental mapping indicates the uniform distribution of C, N, K, Mn, and Fe within the PNPs.

Thermogravimetric analysis (TGA) was employed to investigate the water content in the KMnFe-PBAs (Figure 3, a). TGA data showed several steps of weight loss: the adsorbed water molecules are eliminated at a temperature up to 150 °C and the interstitial water molecules are removed at the temperature range of 150–250 °C. Determined from TGA data, the adsorbed water contents were found to be 1.77 and 2.13 wt.% for PNPs and PBHs, respectively. It is evident that PBHs, with their larger surface area, have more adsorbed water molecules than the PNPs. The interstitial water content in PNPs was measured at 0.24 wt. %, approximately one third of the water contents in PBHs. The low water content in PNPs implies that PNPs have low defects and high crystallinity since the defects such as $[Fe(CN)_6]$ vacancies will cause the empty cavities of $MnFe(CN)_6$ framework that are easily occupied by water molecules. In other

words, lower defects in the PNP structure translates to a lower content of the interstitial water and the enhanced crystallinity. The crystal structures of PNPs were examined by X-ray diffraction (XRD) and presented in Figure 3, b. All diffraction lines in XRD patterns were well-indexed into high-purity monoclinic phase of $K_2Mn[Fe(CN)_6]$ without any impure crystalline phase, indicating a high crystallinity of PNPs.^[1f,8] To investigate the effect of particle size, morphology, and surface area, porosities of the PBAs were analyzed using nitrogen gas sorption analysis. The N_2 adsorption-desorption isotherms of PNP exhibit a type IV profile with a type H₃ hysteresis loop in the relative pressure range of 0.45–1.0, implying the aggregation of non-rigid plate-like particles with slit-shaped pores.^[10] The Brunauer-Emmett-Teller (BET) specific surface area was determined to be $6.8 \text{ m}^2 \text{ g}^{-1}$ for PNPs and $13.8 \text{ m}^2 \text{ g}^{-1}$ for PBHs, indicating that PNPs have a reduced surface area due to their larger particle size (Figure 3, c). Pore distribution analysis indicates that PNPs have a lower quantity of micro- and mesopores on the surface, consistent with the formation of large particles of thin plates and the existence of aggregated plates. The smaller surface area of the PNPs is expected to minimize the occurrence of side reactions during electrochemical reaction, thereby enhancing the cycling stability of the cell.

The electrochemical performances of the PNPs were evaluated in a potassium metal half-cell with an electrolyte of 0.7 M KPF_6 in EC/DEC (1:1, v/v%), and studied through cyclic voltammetry (CV) and galvanostatic charge-discharge (Figure 4).

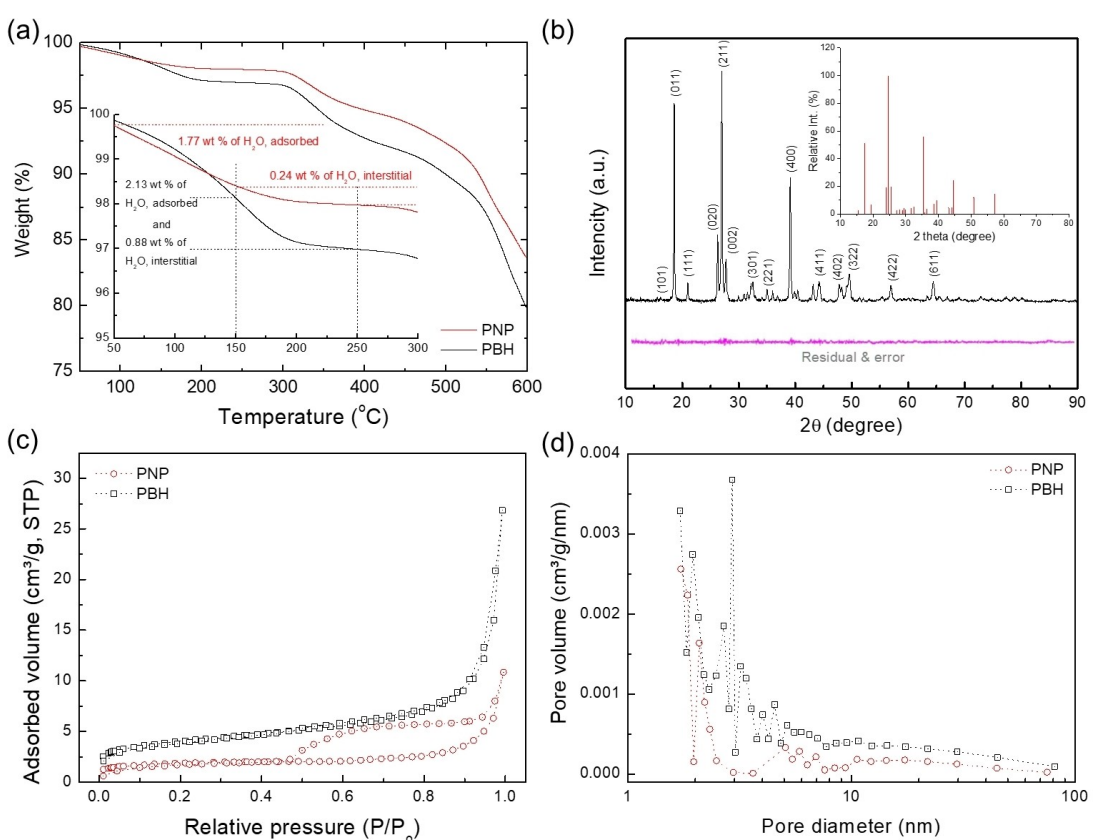


Figure 3. Structural and porosity characterization: (a) TGA curves of PNPs and PBHs, (b) XRD pattern of PNPs, (c) N_2 adsorption-desorption isotherms, and (d) BJH plots of PNPs and PBHs.

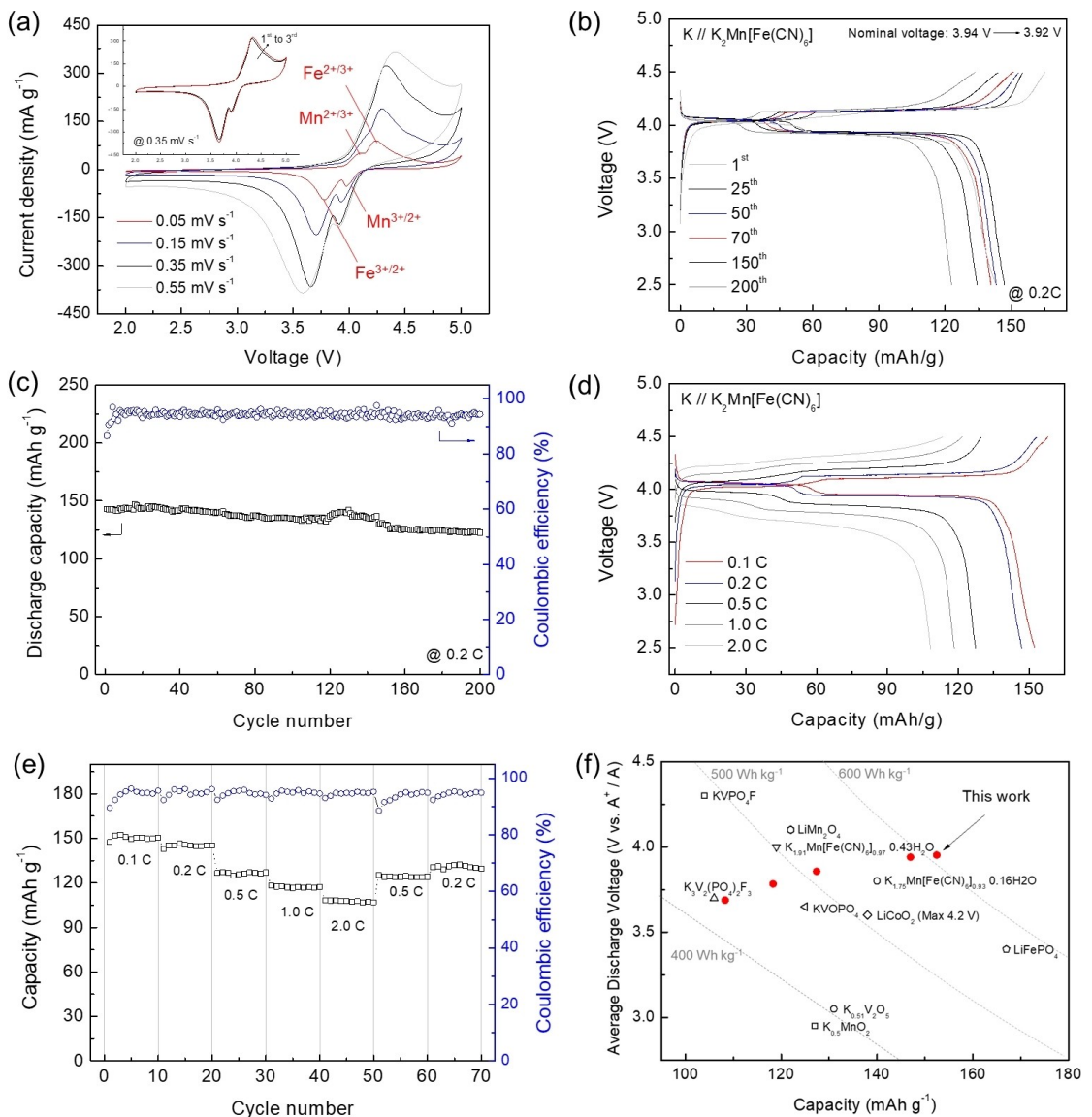


Figure 4. Electrochemical test in a K-metal half-cell: (a) CV curves of PNP at 0.05–0.55 mVs⁻¹, (b) charge-discharge curves of PNP, (c) cyclic performance of PNP, (d) charge-discharge curves at 0.1–2.0 C, (e) rate capabilities at 0.1–2.0 C, and (f) capacity and average voltage plot with comparison to literature values.

Cyclic voltammetry curves indicated that PNP-based cathode undergoes reversible redox reactions with K-ion at scan rates of 0.05–0.55 mVs⁻¹ (Figure 4a). At a scan rate of 0.05 mVs⁻¹, the PNPs show distinct oxidation peaks at 4.09 and 4.23 V, while the corresponding reduction peaks at 3.78 V and 3.98 V, attributed to the redox reaction of Fe^{2+/3+} and Mn^{2+/3+} couples, respectively. These reversible redox reactions were presented on the CV curves at 0.35 mVs⁻¹, with no significant difference in redox voltage between the first and third cycle. (Figure 4a, inset). Electrochemical performances of PNPs and PBHs were compared using CV curves, revealing that the current density of PNPs is significantly higher than that of PBHs at 0.35 mVs⁻¹, suggesting a higher capacity of PNPs (Figure S5). Galvanostatic charge-discharge profile of the PNPs-based cathodes exhibits two distinct voltage plateaus within the potential range of 3.8–4.2 V versus K/K⁺ during charge (depotassiation) and discharge

(potassiation) process, attributed to the Fe^{2+/3+} and Mn^{2+/3+} redox couples. (Figure 4b) As shown in Figure 4b, PNPs showed the maximum discharge capacity of 147.0 mAhg⁻¹ at 0.2 C, approaching the theoretical value of stoichiometric K₂Mn[Fe(CN)₆], and an average discharge potential around 3.940 V. These values are much higher than those obtained with PBHs, as the PBHs showed a capacity of 126 mAhg⁻¹ and a voltage of 3.900 V (Figure S6). The high capacity and redox potential of the PNPs are attributed to their high crystallinity and low content of defects and water. The discharge capacity of the PNP was 143.7 mAhg⁻¹ with an initial Coulombic efficiency (C.E) of 86.6% at the first cycle, and gradually increased to a maximum of 147.0 mAhg⁻¹ with a C.E of 95.8% after 25 cycles. Upon further cycling, the discharge capacity of PNPs slightly decreased to 140.8 mAhg⁻¹ after 70 cycles, and maintained at 134.5 mAhg⁻¹ after 150 cycles. Cycling performance of the PNP-

based cathode was evaluated at 0.2 C. (Figure 4c) It demonstrates an impressive cycling stability with a high capacity retention, maintaining a capacity of 122.9 mAh g^{-1} after 200 cycles. The PNPs also shows a stable average discharge potential of 3.920 V after 200 cycles, suggesting highly stable redox reactions. In addition to high capacity and cycling stability, PNPs shows a high rate capability (Figure 4d). It delivers capacities of 152.5, 147.0, 127.5, 118.3, and 108.3 mAh g^{-1} at C-rates of 0.1, 0.2, 0.5, 1.0, and 2.0 C respectively. Figure 4e also displays a good rate capability of PNPs, demonstrating the capacity retention of 96.4, 83.6, 76.7, and 70.5% at 0.2, 0.5, 1.0, and 2.0 C, respectively. High rate capabilities of PNPs are ascribed to the fast K-ion transport within the PNP crystal structures. When the C-rate was set back to 0.2 C, the capacity recovered from 70.5% to 90.4%, suggesting the structural stability of PNPs. Electrochemical impedance spectroscopy (EIS), and Nyquist plots indicate that the PNPs shows the electrolyte resistance (R_{er}) and reaction resistance (R_{ct}) much smaller than those of PBHs, suggesting that low number of defects and water in the PNPs facilitate K-ion transport in the PNP framework, leading to a lower

polarization, fast kinetics, and superior rate capability (Figure S7). Owing to its high capacity (152.5 mAh g^{-1} at 0.1 C) and high nominal voltage (3.952 V), the PNPs can deliver an energy density of 602.7 Wh kg^{-1} , which is among the highest values reported for PBA-based cathodes (Figure 4f).^[8,11]

A K-ion full-cell was assembled with a natural graphite anode and the PNP-based cathode, using electrolytes of 0.7 M KPF_6 in EC:DEC (1:1, v/v%) and evaluated in a broad voltage ranging from 1.5 to 4.5 V. (Figure 5a). The PNPs // graphite full cell delivers a maximum capacity of 134.2 mAh g^{-1} with a high nominal voltage of 3.958 V. (Figure 5b). The full cell shows an discharge capacity of 120.6 mAh g^{-1} with a C.E. of 74.4% during 1st cycle. Over the following several cycles, the capacity of the full cell gradually increased and reached to a maximum capacity of 132.4 mAh g^{-1} with a C.E. of 98.6% after 20 cycles. High capacity was maintained at 35th cycles with the capacity of 132.6 mAh g^{-1} and C.E. of 98.8%. A slight decay in capacity was observed at the 70th cycle demonstrating a capacity of 123.4 mAh g^{-1} , and the final capacity at the 100th cycle was 108 mAh g^{-1} of capacity with a C.E. of 99.2%. It is noteworthy that the PNPs // graphite full cell stably operates in the voltage

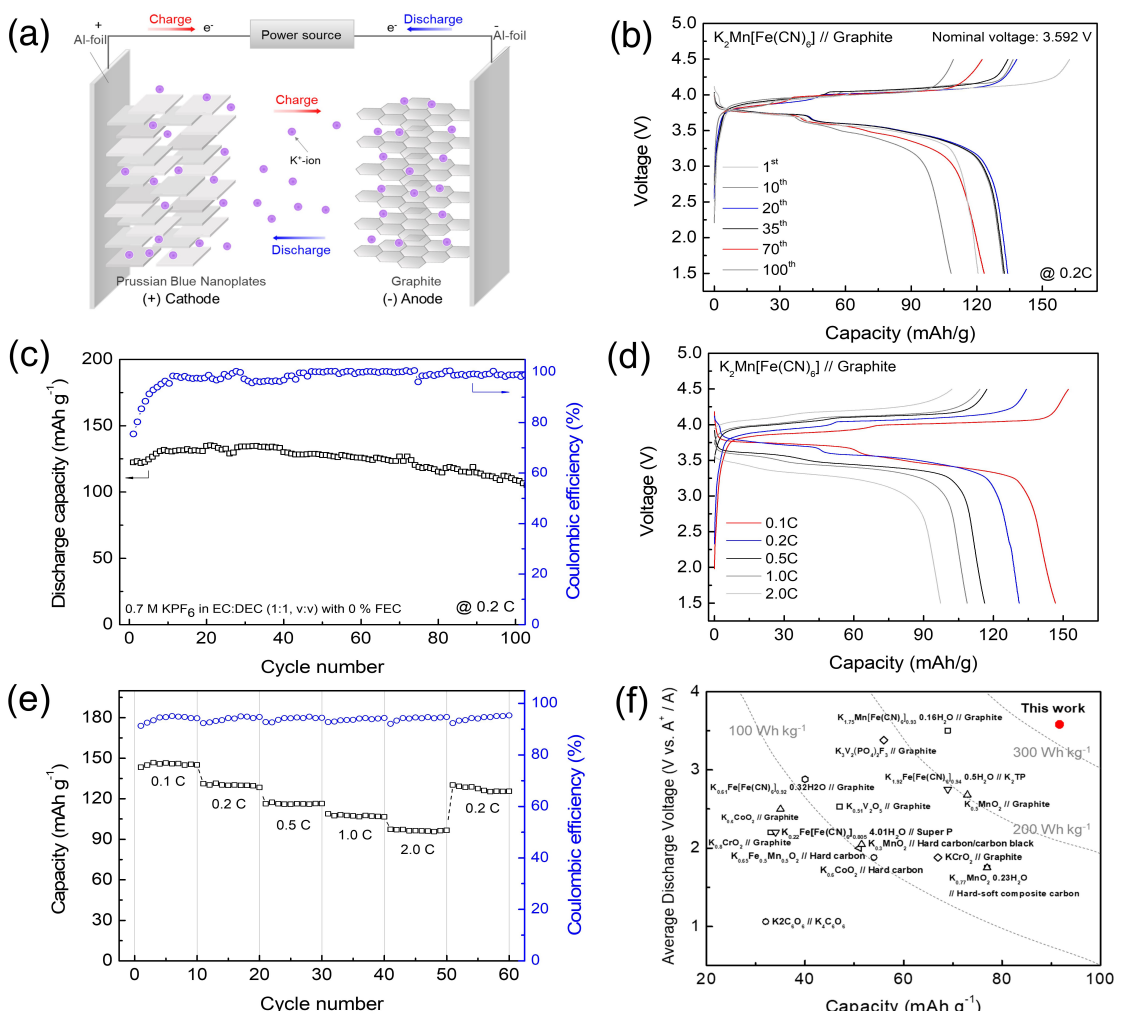


Figure 5. Electrochemical test on full-cell: (a) Schematic illustration of PNPs // Graphite full-cell, (b) charge-discharge curves at 0.2 C, (c) cyclic performance of the full-cell at 0.2 C, (d) charge-discharge curves at 0.1–2.0 C, (e) rate capabilities at 0.1–2.0 C, and (f) capacity and average voltage plot with comparison to literature values.

range of 1.5–4.5 V, while the electrolyte is susceptible to the degradation and side reaction at a high voltage. The PNPs // graphite full cell present a good cycling stability with a high capacity retention and high C.E (Figure 5c). The PNPs // graphite full cell also demonstrates good rate capability. (Figure 5d) Reversible capacities of 146.7, 134.2, 117.3, 108.7, and 97.3 mAhg⁻¹ were obtained at C-rates of 0.1, 0.2, 0.5, 1.0, and 2.0 C, respectively, demonstrating a high rate capability of the full cell. The rate performance of the full cell is presented in Figure 5e, reaching a capacity retention of 91.4, 79.9, 74.0 and 66.3% at C-rates of 0.2, 0.5, 1.0, and 2.0 C, respectively. The discharge capacity returned back to 91.4% when C-rate recovered to 0.2 C, demonstrating its good rate capability. Moreover, the full cell delivered a reversible capacity of 91.7 mAhg⁻¹ based on the total mass of the cathode and anode materials. Owing to its high capacity and high voltage, the PNPs // graphite full cell can achieve an energy density of 328.3 Wh kg⁻¹, which is among the highest value reported for K-ion full cell. (Figure 5f).^[8,11]

Conclusions

In conclusion, we synthesized a potassium manganese hexacyanoferrate Prussian blue analogues with a thin plate-like morphology and explored their potential as positive electrode materials for K-ion battery. Prussian blue plates (PNPs) were synthesized through a precipitation reaction in a high-concentration potassium citrate solution, resulting in low content of defects and water within the crystal structure. In a K-metal half-cell, the as-prepared PNPs exhibits a high capacity of 152.5 mAhg⁻¹ and a nominal voltage of 3.952 V, with an energy density of 602.7 Wh kg⁻¹. The PNPs yielded a reversible discharge capacity of 147.0 mAhg⁻¹ at 0.2 C and retain high capacity over 200 cycles. Moreover, a full-cell constructed by combining PNP cathode with graphite anode delivered a maximum capacity of 146.7 mAhg⁻¹ with a good cycling stability over 100 cycles. With high capacity and nominal voltage, the PNP-utilized full-cell achieved a high cell energy density of 328.3 Wh kg⁻¹ per both electrodes, indicating the potential of PNPs as a promising cathode material for potassium ion batteries.

Notes

The authors declare none of financial interest.

Acknowledgements

This work was supported by the National Research Foundation of Korea (NRF) grant funded by the Korea government (MSIT) (No. 2022R1 A2 C1093082). This work was supported by the Gachon University research fund of 2019 (GCU-2019-0832).

Conflict of Interests

The authors declare no conflict of interest.

Data Availability Statement

Research data are not shared.

Keywords: Prussian blue analogue • potassium manganese hexacyanoferrate • plate-like nanoparticles • potassium ion battery

- [1] a) T. Hosaka, K. Kubota, A. S. Hameed, S. Komaba, *Chem. Rev.* **2020**, *120*, 6358; b) K. Kubota, S. Komaba, *J. Electrochem. Soc.* **2015**, *162*, A2538; c) S. W. Kim, D. H. Seo, X. Ma, G. Ceder, K. Kang, *Adv. Energy Mater.* **2012**, *2*, 710; d) V. Palomares, P. Serras, I. Villaluenga, K. B. Hueso, J. Carretero-González, T. Rojo, *Energy Environ. Sci.* **2012**, *5*, 5884; e) S. L. Dreyer, F. M. Maddar, A. Kondrakov, J. Janek, I. Hasa, T. Brezesinski, *Batteries & Supercaps* **2024**, *7*, e202300595; f) Y. Xu, M. Titirici, J. Chen, F. Cora, P. L. Cullen, J. S. Edge, K. Fan, L. Fan, J. Feng, T. Hosaka, *Journal of Physics: Energy* **2023**, *5*, 021502.
- [2] a) S. Zhao, Z. Guo, K. Yan, X. Guo, S. Wan, F. He, B. Sun, G. Wang, *Small Structures* **2021**, *2*, 2000054; b) S. Komaba, T. Hasegawa, M. Dahbi, K. Kubota, *Electrochim. Commun.* **2015**, *60*, 172; c) Z. Jian, W. Luo, X. Ji, *J. Am. Chem. Soc.* **2015**, *137*, 11566; d) W. Luo, J. Wan, B. Ozdemir, W. Bao, Y. Chen, J. Dai, H. Lin, Y. Xu, F. Gu, V. Barone, *Nano Lett.* **2015**, *15*, 7671; e) X. Min, J. Xiao, M. Fang, W. A. Wang, Y. Zhao, Y. Liu, A. M. Abdelkader, K. Xi, R. V. Kumar, Z. Huang, *Energy Environ. Sci.* **2021**, *14*, 2186; f) H. Huang, X. Wu, Y. Gao, Z. Li, W. Wang, W. Dong, Q. Song, S. Gan, J. Zhang, Q. Yu, *Adv. Energy Mater.* **2024**, *36*, 2304251; g) K. Sada, J. Darga, A. Manthiram, *Adv. Energy Mater.* **2023**, *13*, 2302321.
- [3] H. Park, Y. Lee, W. Ko, M. Choi, B. Ku, H. Ahn, J. Kim, J. Kang, J. K. Yoo, J. Kim, *Batteries & Supercaps* **2023**, *6*, e202200486.
- [4] a) H. Kim, D. H. Seo, M. Bianchini, R. J. Clément, H. Kim, J. C. Kim, Y. Tian, T. Shi, W. S. Yoon, G. Ceder, *Adv. Energy Mater.* **2018**, *8*, 1801591; b) V. Mathew, S. Kim, J. Kang, J. Gim, J. Song, J. P. Baboo, W. Park, D. Ahn, J. Han, L. Gu, *NGP Asia Mater.* **2014**, *6*, e138; c) N. Recham, G. I Rousse, M. T. Sougrati, J.-N. I Chotard, C. Frayret, S. Mariyappan, B. C. Melot, J.-C. Jumas, J.-M. Tarascon, *Chem. Mater.* **2012**, *24*, 4363; d) W. B. Park, S. C. Han, C. Park, S. U. Hong, U. Han, S. P. Singh, Y. H. Jung, D. Ahn, K. S. Sohn, M. Pyo, *Adv. Energy Mater.* **2018**, *8*, 1703099; e) Y.-H. Zhu, Q. Zhang, X. Yang, E.-Y. Zhao, T. Sun, X.-B. Zhang, S. Wang, X.-Q. Yu, J.-M. Yan, Q. Jiang, *Chem* **2019**, *5*, 168; f) K. Sun, S. H. Luo, G. Hao, S. Guo, L. L. Qian, S. x Yan, Q. Wang, *The Chemical Record* **2024**, *24*, e202300327; g) T. Masese, G. M. Kanyolo, *Energy Advances* **2024**, *3*, 60.
- [5] a) L. Xue, Y. Li, H. Gao, W. Zhou, X. Lü, W. Kaveevivitchai, A. Manthiram, J. B. Goodenough, *J. Am. Chem. Soc.* **2017**, *139*, 2164; b) K. Hurlbutt, S. Wheeler, I. Capone, M. Pasta, *Joule* **2018**, *2*, 1950; c) H. Yi, R. Qin, S. Ding, Y. Wang, S. Li, Q. Zhao, F. Pan, *Adv. Funct. Mater.* **2021**, *31*, 2006970.
- [6] A. Eftekhar, *J. Power Sources* **2004**, *126*, 221.
- [7] a) L. Deng, J. Qu, X. Niu, J. Liu, J. Zhang, Y. Hong, M. Feng, J. Wang, M. Hu, L. Zeng, *Nat. Commun.* **2021**, *12*, 2167; b) X. Jiang, T. Zhang, L. Yang, G. Li, J. Y. Lee, *ChemElectroChem* **2017**, *4*, 2237.
- [8] X. Bie, K. Kubota, T. Hosaka, K. Chihara, S. Komaba, *J. Mater. Chem. A* **2017**, *5*, 4325.
- [9] a) G. Zeng, S. Xiong, Y. Qian, L. Ci, J. Feng, *J. Electrochem. Soc.* **2019**, *166*, A1217; b) H. Onuma, K. Kubota, S. Muratsubaki, T. Hosaka, R. Tatarra, T. Yamamoto, K. Matsumoto, T. Nohira, R. Hagiwara, H. Oji, *ACS Energy Lett.* **2020**, *5*, 2849; c) Y. Xu, T. Ding, D. Sun, X. Ji, X. Zhou, *Adv. Funct. Mater.* **2023**, *33*, 2211290.
- [10] M. Thommes, K. Kaneko, A. V. Neimark, J. P. Olivier, F. Rodriguez-Reinoso, J. Rouquerol, K. S. Sing, *Pure Appl. Chem.* **2015**, *87*, 1051.
- [11] a) Y.-H. Zhu, X. Yang, D. Bao, X.-F. Bie, T. Sun, S. Wang, Y.-S. Jiang, X.-B. Zhang, J.-M. Yan, Q. Jiang, *Joule* **2018**, *2*, 736; b) C. Zhang, Y. Xu, M. Zhou, L. Liang, H. Dong, M. Wu, Y. Yang, Y. Lei, *Adv. Funct. Mater.* **2017**, *27*, 1604307; c) J. Liao, Q. Hu, Y. Yu, H. Wang, Z. Tang, Z. Wen, C. Chen, J. Mater. Chem. A **2017**, *5*, 19017; d) Q. Zhao, J. Wang, Y. Lu, Y. Li, G. Liang, J. Chen, *Angew. Chem. Int. Ed.* **2016**, *55*, 12528; e) C. Vaalma, G. A. Giffin, D. Buchholz, S. Passerini, *J. Electrochem. Soc.* **2016**, *163*, A1295; f) X.

Wang, X. Xu, C. Niu, J. Meng, M. Huang, X. Liu, Z. Liu, L. Mai, *Nano Lett.* **2017**, *17*, 544; g) T. Deng, X. Fan, C. Luo, J. Chen, L. Chen, S. Hou, N. Eidson, X. Zhou, C. Wang, *Nano Lett.* **2018**, *18*, 1522; h) H. Kim, D.-H. Seo, A. Urban, J. Lee, D.-H. Kwon, S.-H. Bo, T. Shi, J. K. Papp, B. D. McCloskey, G. Ceder, *Chem. Mater.* **2018**, *30*, 6532; i) H. Kim, J. C. Kim, S. H. Bo, T. Shi, D. H. Kwon, G. Ceder, *Adv. Energy Mater.* **2017**, *7*, 1700098; j) T. Deng, X. Fan, J. Chen, L. Chen, C. Luo, X. Zhou, J. Yang, S. Zheng, C. Wang, *Adv. Funct. Mater.* **2018**, *28*, 1800219; k) B. Lin, X. Zhu, L. Fang, X. Liu, S. Li, T. Zhai, L. Xue, Q. Guo, J. Xu, H. Xia, *Adv. Mater.*

2019, *31*, 1900060; l) Q. Yu, J. Hu, W. A. Wang, Y. Li, G. Suo, L. Zhang, K. Xi, F. Lai, D. Fang, *Chem. Eng. J.* **2020**, *396*, 125218.

Manuscript received: February 8, 2024
Revised manuscript received: March 18, 2024
Accepted manuscript online: March 21, 2024
Version of record online: April 17, 2024
